This is the author's version of a work that was submitted/accepted for publication in the following source:

Notice: *Changes introduced as a result of publishing processes such as copy-editing and formatting may not be reflected in this document. For a definitive version of this work, please refer to the published source:*

3D-printed cellular structures for bone biomimetic implants

Sakkadech Limmahakhun[a], Adekunle Oloyede[a], Kriskrai Sitthiseripratip[b], Yin Xiao[a], Cheng Yan[a]*

[a] School of Chemistry, Physics and Mechanical Engineering, Queensland University of Technology (QUT), 2 George Street, Brisbane, QLD 4001, Australia
sakka_lim@hotmail.com; k.oloyede@qut.edu.au; yin.xiao@qut.edu.au; c2.yan@qut.edu.au
[b] National Metal and Materials Technology Centre
114 Thailand Science Park, Pahonyothin Road, Klong Luang, Pathumthani, Thailand
kriskrs@mtec.or.th

* Corresponding author: Tel.: +6 1731386630.
                           Email address: c2.yan@qut.edu.au (C. Yan).

Abstract

The use of porous cellular structures in bone tissue engineering can provide mechanical and biological environments closer to the host bone. However, poor internal architectural designs may lead to catastrophic failure. In this work, 192 open-porous cellular structures were fabricated using 3D printing (3DP) techniques. The mechanical and biological behavior of four 3D internal structures (octahedral, pillar octahedral, cubic and truncated octahedral) was investigated. It was found that the pillar octahedral shape has not only greater stiffness and strength under compression, shear and torsion but increased rate of pre-osteoblastic cell proliferation. We believe bone implants can be fabricated using 3DP techniques and their mechanical and biological performance can be tailored by modifying the internal architectures.

Keywords: Cellular structures, 3D printing, Stiffness, Strength, Bone implants

1. Introduction

Bone implants have been increasingly used to repair the defects of host bones. One promising approach is creating three-dimensional (3D) porous cellular structures that provide suitable microenvironments to achieve required osseointegration. Both porosity and pore size have direct influence on their functionalities for biomedical applications [1, 2]. Many biocompatible polymers such as polycaprolactone (PCL) and chitosan have been used in bone tissue regeneration as a temporary scaffold to facilitate bony ingrowth. However, their low mechanical strength limits their applications for load-bearing implants [3-5].

Polyurethane (PUR) is a biostable, biocompatible polymer [6]. Its hydrolytic stability leads to limited degradability which makes PUR less suitable for bone regenerations. On the other hand, the excellent loading bearing capacity and bio-stablility make this material a choice for prostheses. In vivo practice of using PUR scaffold to repair bone defects have demonstrated its potential for applications in osseointegratable implants [7].

Besides the intrinsic material properties of the polymers, the internal architecture of a cellular structure has significant effect on its mechanical and biological behaviors [8]. Improved specific mechanical properties have been observed in non-stochastic geometries [9-12]. Recently, the advances in additive manufacturing (AM) technologies make it possible to rapidly create cellular structures based on 3D computer-aided design (CAD) models, with good accuracy and reproducibility [8, 13-15].

Sudarmadji, Tarawneh, and Wettergreen created the cellular structures based on the space-filling unit cells of polyhedral shapes and the mechanical performance could be easily

controlled by the unit dimensions [5, 8, 16]. It was reported that a cellular structure with cubic-shape units had similar stiffness and strength (E = 1.06–17.98 GPa and σ = 0.5–350 MPa) as cortical and cancellous bones [13, 17-19]. On the other hand, the cellular structures with bone-equivalent stiffness could also be achieved using octahedral-shape units [20-22]. It is not clear what types of internal architectures should be adopted for bone implants.

In general, smaller pore sizes may prevent cell penetrating within the cellular structures. The porosity and pore size are related to the internal unit structures. The mechanical response of polyhedral-shape units has been investigated under uniaxial compression but the role of loading mode has not been well understood. Up to now, few studies have been carried out to investigate the effects of 3D internal architectures on both mechanical and biological behavior.

Considering VisiJet material (3D System, USA) as a derivative of PUR, it is known as one of the tough, biocompatible, biostable polymers and can be processed using AM technologies. It has 3-time greater elastic modulus and strength than PCL [23]. However, it is unknown if this material is suitable for bone biomedical applications especially when fabricated with AM technologies.

In this work, the mechanical and biological performance of cellular structures with different 3D internal architectures under compression, shear and torsion was investigated. The stress relaxation, cell adherence and proliferation tests were also conducted to examine suitability of these structures as the implants.

2. Materials and methods

2.1. Material and 3D printing (3DP)

3D cellular structures were fabricated with a photopolymerizable polymer (VisiJet® M3 Crystal) using 3DP technologies (ProJet® 3500SD, 3D Systems). This polymer, composed of urethane acrylate oligomers, has been certified by United States Pharmacopeia (USP) as Class VI material. It is the strictest class for plastic biocompatibility and has a tensile modulus of 1.594 GPa and tensile strength of 35.2 MPa, which are closer to the trabecular bone, i.e., 2.73 ± 1.06 GPa and 18 ± 6.4 MPa, respectively [24]. The 3DP process can achieve an accuracy/layer thickness of 50/30 μm and requires hydroxylated wax as a supporting material (VisiJet® S300) during the printing. The wax was then removed afterwards via melting at 70°C and multi-step cleaning with 99% isopropanol.

2.2. 3D cellular structures

For comparison, different 3D internal architectures were designed using a CAD software (SolidWorks 15, USA) to achieve (1) no enclosed pores after unit cell replication, (2) different strut orientations [0°/45°/90°] along the loading directions, or (3) internal architecture similar to trabecular bone. Based on polyhedral geometries, four 3D internal architectures were designed, i.e., octahedral [± 45°], pillar octahedral [0° ± 45°], cubic [0° ± 90°], and truncated octahedral shapes.

In Fig. 1a, the unit dimension (L) is 2 mm and strut size (t) is 400 μm and 500 μm. The cellular structures were designed and fabricated by repeating these unit cells along x, y, and z axes. Rectangular (10 x 20 mm) and cylindrical (10 x 30 mm) cellular structures were prepared to investigate the mechanical properties, Fig. 1c.
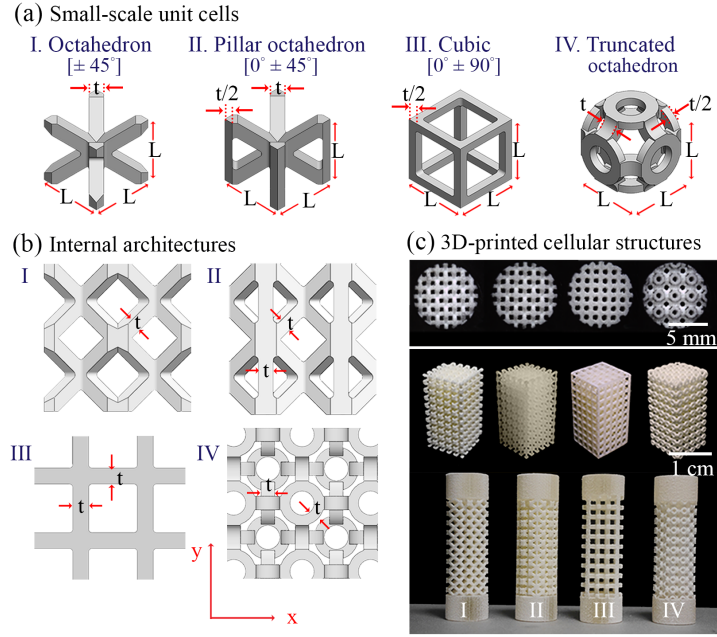
Fig. 1. The designs of open-porous cellular structures with different internal architectures: (I) octahedron [± 45°], (II) pillar octahedron [0° ± 45°], (III) cubic [0° ± 90°], and (IV) truncated octahedron. (a) small-scale unit cells (L = 2 mm), (b) internal architectures created by unit cells with the strut sizes (t) of 400 µm and 500 µm, (c) final models manufactured using 3DP methods used for cell cultures (top) and mechanical testing (middle and bottom).

2.3. Characterization of morphology

The actual morphology of these cellular structures were characterized using helium gas pycnometry (Pentapyc 5200e, Quantachrome) and scanning electron microscopy (SEM, Quanta 200, FEI). The skeletal density of the specimens was calculated as its weight per unit skeletal volume [25], and the relative density (ρ^*/ρ_s) was estimated by the ration between the density of cellular structures (ρ^*) and the material (ρ_s = 1.02 g/cc). The overall porosity was evaluated as the ratio of the total volume of voids to the total volume of the cellular structure [26]. The morphology and sizes were also interpreted using SEM. The pore size is determined by the shape of the unit cells and t as L was fixed.

2.4. Mechanical tests

The total of 108 cellular structures were tested for mechanical performances. Quasi-static compression, shear, and torsion were conducted with a strain rate of 1 mm/min (INSTRON 5985). A specially designed torsion fixture was fitted into a 500 N load cell. It can be operated in ± 45° angular displacement with a resolution of 0.001°. The compressive, shear, and torsional stiffness was determined from the initial linear portion of the stress-strain curves. The failure strength in compression (σ_{fail}), shear (T_{fail}), and torque was recorded at the peak loads.

The four architectures with t = 500 µm were selected to conduct stress relaxation tests. Three specimens were tested for each structure. Two different environmental conditions were used, including dry and wet conditions at room temperature (25°C). All wet tests were conducted by immersing the specimens in PBS for 1 hour prior to the test. Quasi-static compression was conducted up to the failure point. With a total strain of 2.5%, the stress relaxation test was carried out in 5 steps, at a strain rate of 0.25% s^{-1} for 2 s (ramp) and followed by 58 s relaxation (hold).

2.5. Cell cytotoxicity, adherence, and proliferation

The L and t in individual unit cells can be adjusted to achieve similar strut, pore size, and porosity for the four architectures. The new CAD models have a surface area of 31.58, 33.47, 26.91, and 33.21 mm^2 for the octahedral, pillar octahedral, cubic, and truncated octahedral structure, respectively. The total of 84 disc-shape scaffolds with a diameter of 8 mm, a height of 2 mm were remodeled and manufactured, exhibiting a mean t of 453 ± 36 μm, pore size of 551 ± 55 μm, and porosity of $74 \pm 4\%$ ($p = 0.12$, 0.69, and 0.82, respectively), Fig. 1c.

Murine pre-osteoblastic cells, MC3T3-E1, (passage 6) were cultured in D-MEM (Gibco) supplemented with 10 % fetal bovine serum (FBS, Gemini) and 1% Penicillin/Streptomycin (Gibco) at 37°C in a 5% CO2 incubator. Proliferation media were changed every 2-3 days, the subconfluent cells were detached using 0.25% trypsin EDTA (Gibco), and then centrifuged, re-suspended and counted.

All disc-shape scaffolds were sterilized with 70% ethanol overnight and rinsed three times with sterile phosphate-buffered saline (PBS), then dried under UV tissue culture hood. Biocompatibility of the 3DP parts was first tested in 7 days by adopting indirect cell-culture techniques. The cell survival rates of the 3DP specimens were calculated using the ratio of cell viability to the seeded-cells. Then cells were directly seeded onto the scaffolds at a density of 5×10^4 cells/scaffold and allowed to adhere to the scaffold overnight in 250 ml of proliferation media in a 48-well tissue culture plate. The scaffolds were placed into the new plate in the following day, which denoted as the day 1. The cell-seeded scaffolds were harvested on day 1, 4 and 7. The survival rate, cell adherence and proliferation were quantified by DNA assay (CyQuant NF, Invitrogen) at different time points.

The pre-osteoblastic cell morphologies were evaluated with SEM. After removing from the culture media, these scaffolds were rinsed twice with PBS and fixed with 3% glutaraldehyde. Then, the scaffolds were further rinsed with 0.1 M cacodylate buffer, followed by post-fixation with 1% osmium tetroxide for 1 h. After rinsing with demineralized water, the scaffolds were subsequently dehydrated using graded ethanol of 50, 70, 90 and 100%, then immersed twice into hexamethyldisilazane (HMDS, Sigma) for 30 min each and left for drying overnight before an inspection with SEM.

2.6. Data analysis

Descriptive and analytical approaches were used in the data analysis. Paired t-tests assessed significant differences of the stiffness acquired with dry and wet condition. One-way ANOVA was used to test for significant differences in each independent factor between the four architectures. Two-way ANOVA was used to test for significant differences in stepped stress-relaxation tests. The independent factors in this two-way ANOVA were time and the condition applied. Statistical analysis was performed in SPSS v21 (IBM Corp, USA) and the significance threshold was set to $p \leq 0.05$.

3. Results and discussion

3.1. Cellular structures fabricated using 3DP

3DP techniques used powder-based polymer and wax-like material as the support material to fabricate the cellular structures. Strut orientations [0°/45°/90°] of a unit cell affected the density of the 3DP cellular structures (Table 1). A cube-shaped unit cell, presenting the horizontal [0°] and vertical [± 90°] struts along the building axis, had a greater density than unit cells whose struts aligned in an inclination [± 45°] ($\rho = 1.36 \pm 0.02$ g/cc and 1.19 ± 0.02 g/cc). By contrast, 3DP cellular structures with the ± 45° struts exhibited a greater porous surface than the cube-shaped unit, as a result of the stair-stepping effect [27] associated with powder-based fabrication methods. Therefore, the strut density fabricated

with 3DP techniques varied with the degrees between strut alignment and building axis. The 3DP techniques, in this work, created a surface pore of 40 μm especially on the overhanging features, as shown in Fig. 10c.

Table 1 Design and actual morphological features of the cellular structures.

Types	Design parameters			Actual parameters ($n = 5$)			Density (g/cc)
	Strut size (μm)	Pore size (μm)	Porosity (%)	Strut size (μm)	Pore size x, y (μm)	Porosity (%)	
Octahedron	400	870	76.6	460 ± 19	606 ± 50	73.15 ± 2.2	1.19 ± 0.01
	500	730	65.9	530 ± 13	421 ± 62	61.35 ± 2.4	
Pillar octahedron	400	870	73.7	460 ± 21	625 ± 48	69.79 ± 3.4	1.18 ± 0.02
	500	730	62.1	583 ± 37	426 ± 45	53.82 ± 3.3	
Cubic	400	1,600	83.7	450 ± 31	2,042 ± 84	87.65 ± 2.4	1.36 ± 0.02
	500	1,500	78.2	535 ± 21	1,695 ± 130	80.61 ± 2.5	
Truncated octahedron	400	700	73.3	435 ± 34	348 ± 59	74.14 ± 3.1	1.21 ± 0.02
	500	700	68.7	508 ± 38	269 ± 25	63.60 ± 3.3	

The cellular structures fabricated with 3DP techniques yielded similar strut sizes for each polyhedral shape ($p = 0.65$ and 0.07 for t = 400 μm and 500 μm). The design strut size (t) of 400 μm and 500 μm offered the pore sizes in the x, y direction between 269 μm to 1,695 μm and resultant porosities ranged from 53.82% to 87.65%.
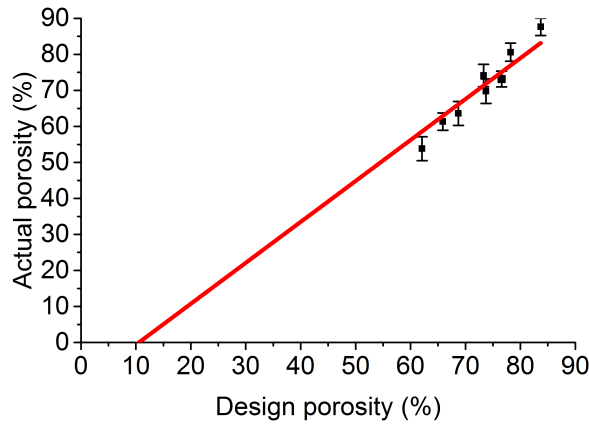

Fig. 2. Correlation between the target component design porosities and actual design porosities of different internal architectures. A least-square regression line is fit to the data to show correlation.

The design and actual porosities fabricated with 3DP are in good agreement, as shown in Fig. 2. However, the least-squares regression fit did not pass through the origin, illustrating that the manufactured porosity was consistently 12% less than the design porosity for the cellular structures. The cellular structures fabricated with 3DP techniques here had a greater accuracy for controlling porosity ($R^2 = 0.902$, standard error (SE) 12%) than those fabricated with selective laser sintering (SLS) techniques ($R^2 = 0.8611$, SE 27.8%) [13].

3.2. Mechanical tests
The mechanical behavior of polyhedral unit cells was investigated under uniaxial compression [8, 16, 28]. This study showed that only compression was insufficient to interpret the overall performances of these units. The mechanical behaviors of the four

internal architectures under different loadings are shown in Table 2. It is clear the strut size, t and the geometries all affect the mechanical properties in compression, shear, and torsion.

Table 2 Mechanical properties of the cellular structures.

	Compression		Shear		Torsion	
	Stiffness (MPa)	σ_{fail} *(MPa)*	*Stiffness (MPa)*	T_{fail} *(MPa)*	*Stiffness (N.mm/θ)*	*Torque (N.mm)*
Strut size (t = 400 μm)						
Octahedron	2.47 ± 0.3	0.25 ± 0.05	2.92 ± 0.07	0.23 ± 0.01	4.33 ± 0.24	69.2 ± 40
Pillar Octahedron	15.26 ± 0.9	0.65 ± 0.10	9.87 ± 0.09	0.31 ± 0.02	5.48 ± 1.82	78.9 ± 24
Cubic	31.44 ± 0.3	0.24 ± 0.01	0.14 ± 0.10	0.09 ± 0.01	0.71 ± 0.29	17.1 ± 10
Truncated Octahedron	6.37 ± 0.1	0.19 ± 0.03	2.66 ± 0.03	0.11 ± 0.01	1.70 ± 0.47	36.6 ± 8
Strut size (t = 500 μm)						
Octahedron	16.80 ± 0.9	1.02 ± 0.8	8.08 ± 0.05	0.38 ± 0.03	9.43 ± 0.50	200.2 ± 22
Pillar Octahedron	26.94 ± 0.4	1.69 ± 0.02	18.93 ± 0.2	0.56 ± 0.02	9.52 ± 0.68	156.3 ± 30
Cubic	59.76 ± 0.5	1.01 ± 0.07	2.59 ± 0.04	0.17 ± 0.02	1.07 ± 0.64	26.9 ± 12
Truncated Octahedron	25.14 ± 0.2	0.72 ± 0.1	7.96 ± 0.02	0.31 ± 0.01	2.20 ± 0.49	43.9 ± 18

Fig. 3 shows the stiffness of the cellular structure with t = 500 μm. The cubic unit cell has the greatest stiffness under compression (59.76 MPa) but its stiffness under shear and torsion is very low (2.59 MPa & 1.07 MPa, respectively). The octahedron and truncated octahedron have similar shear stiffness. Compared with the truncated octahedral type, the octahedron has a greater torsional stiffness (9.43 MPa vs 2.2 MPa) but a lower compression stiffness (16.80 MPa vs 25.14 MPa). In contrast to the octahedron, the pillar octahedron exhibits increased compressive stiffness (26.94 MPa). It also has the greatest shear and torsional stiffness (18.93 MPa and 9.52 MPa, respectively). Because of the vertical struts combined with the ±45° struts in octahedral unit cells, the pillar octahedron [0°, ±45°] is the best internal architecture in terms of stiffness and strength subject to compression, shear, and torsion.
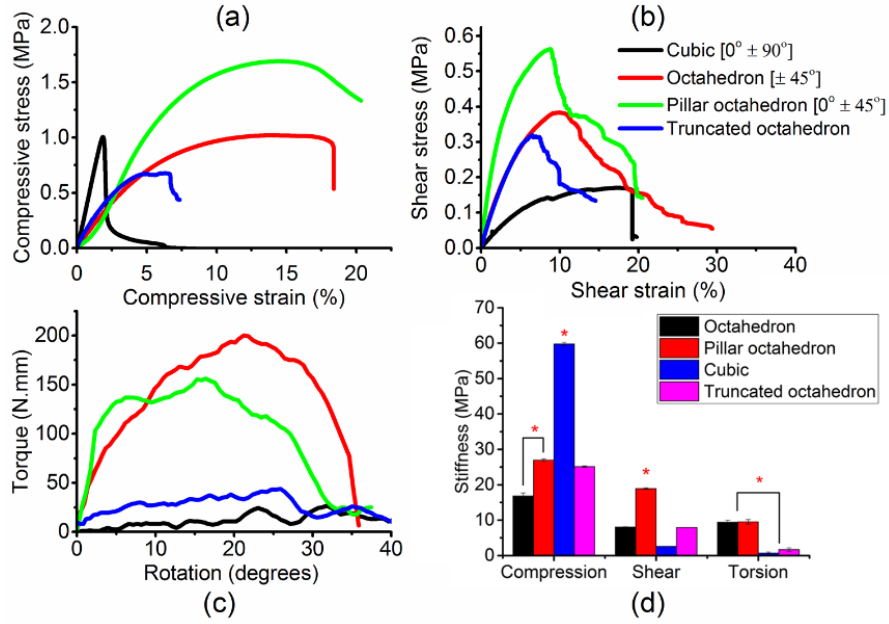
Fig. 3. Stress-strain curves of cellular structures under (a) compression, (b) shear and (c) torsion. The structural stiffness is shown in (d).

The failure modes of these cellular structures under compression are shown in Fig. 4. Buckling occurs in the cubic unit cell before the final failure. By contrast, deformation in the octahedral and truncated octahedral unit cells is dominated by shear band at about 45°. The advantages of the vertical struts in pillar octahedral unit cells include stronger resistance to buckling and improved stiffness and failure strength under shear and torsion loads.
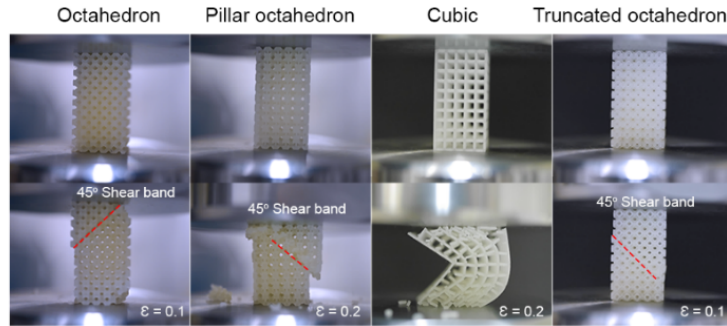

Fig. 4. Deformation modes of cellular structures (t = 500 µm) at strains of 0.1 and 0.2.

The relationship between stiffness of cellular structures in compression (E^*) and porosity (φ) was studied. Based on Gibson and Ashby model [29], they can be correlated as

$$E^* = Es(1-\varphi)e^{C\varphi} \qquad (1)$$

where Es is the elastic modulus of material (1,539 MPa for VisiJet) and C is a constant dependent on the geometry. Fitting this equation with the experimental data, the C for octahedral, pillar octahedral, cubic, and truncated octahedral unit cells (L = 2 mm) is -6.513, -5.339, -2.023, and -5.286, respectively. The estimated E^* with porosity is shown in Fig. 5. Obviously, the cubic structure has the highest modulus in compression, consistent with the experimental observation.
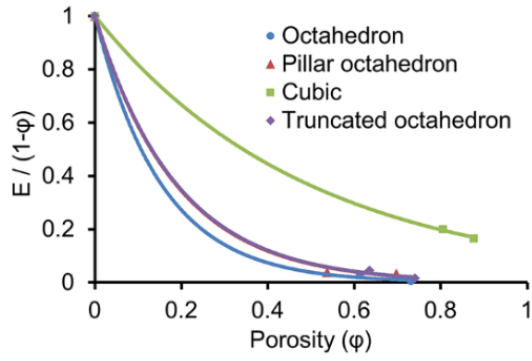
Fig. 5. Variation of effective elastic modulus with porosity.

On the other hand, the viscoelastic properties, often observed in biological or wet environments are important for the materials to be used as implants. Thus, mechanical tests under wet condition and stress relaxation tests were conducted. After immersing these 3D cellular structures into PBS solution, to different extent, the compressive stiffness is reduced, as shown in Fig. 6. For octahedron, pillar octahedron, and truncated octahedron structures, increased ductility (elongation > 30%) was achieved but for the cubic shape, the ductility was less than 5%, similar to that under dry condition.
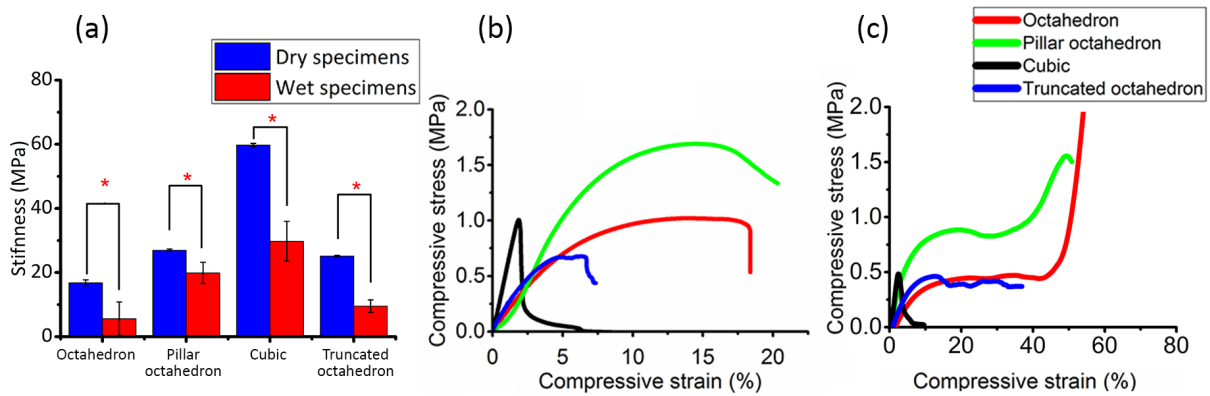

Fig. 6. (a) Stiffness under dry and wet conditions, (b) stress-strain curves under dry condition and (c) stress-strain curves under wet condition.

Under both dry and wet conditions, the stress relaxation test was carried out in 5 steps, at a strain rate of 0.25% s^{-1} for 2 s (ramp) and followed by 58 s relaxation (hold). All the cellular structures showed the progressive increase in stress with strain except the cubic structure at the last step due to the cracking. As shown in Fig. 7, the pillar octahedral structure has the greatest accumulated stress up to 0.63 ± 0.07 MPa and 0.44 ± 0.05 MPa under dry and wet conditions, but less than 0.3 MPa for octahedron and truncated octahedron structures.
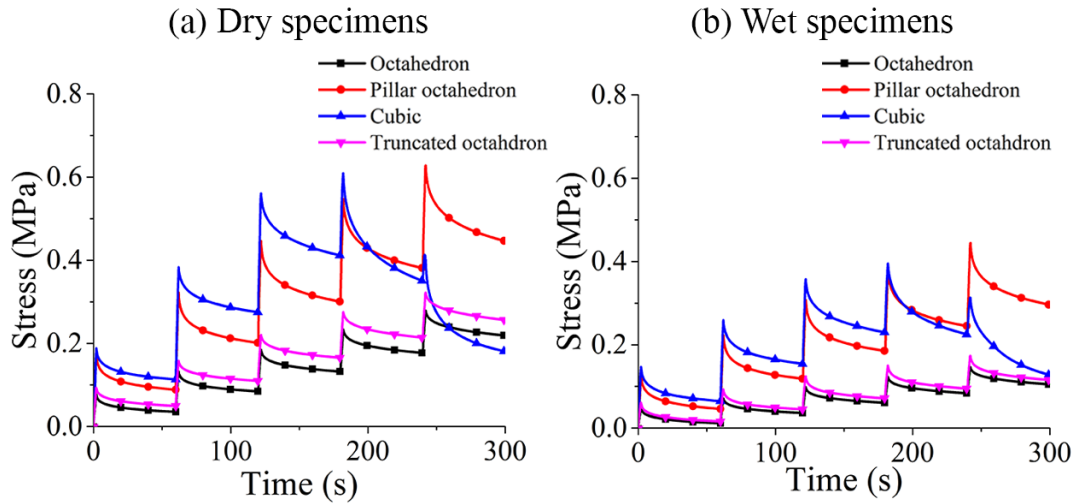
Fig. 7. Stress relaxation behavior under (a) dry and (b) wet conditions of 3DP cellular structures.

Fig. 8 shows the relaxation rate for the first stage. The octahedral, pillar octahedral, and truncated octahedral structures are relaxed up to 50% and the cubic is relaxed up to 40% in dry. The relaxation rate is increased under the wet condition in all structures and the maximum is around about 80%, comparable to the 85% in chitosan scaffolds but much higher than synthetic polymer PCL which has 30% relaxation [30].
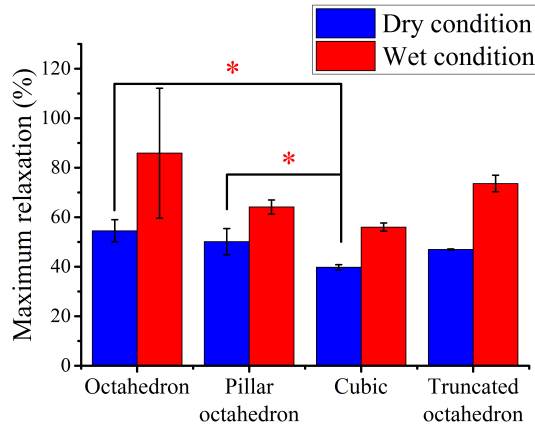

Fig. 8. Maximum stress relaxation corresponding to the first step.

The stress relaxation at different steps can be normalized by translating the stress pattern for each step to its origin based on the quasi-linear viscoelastic theory [31]. The time-dependent stress relaxation function, G(t) can be expressed by

$$G(t) = \sigma(t)/\sigma^e(\varepsilon) \qquad (2)$$

where $\sigma^e(\varepsilon)$ is the maximum stress at each strain (ε) step. The G(t) for both dry and wet condition is shown in Fig. 9 For octahedral, pillar octahedral and truncated octahedral structures, the relaxation is more significant at the first step and gradually weakened at the following steps. However, no consistent trend can be found in the cubic structure. Except the first step, no significant difference in relaxation can be identified between the dry and wet conditions for the octahedral and pillar octahedral structures. By contrast, the relaxation becomes more significant difference for the cubic and truncated octahedral structure under wet condition.
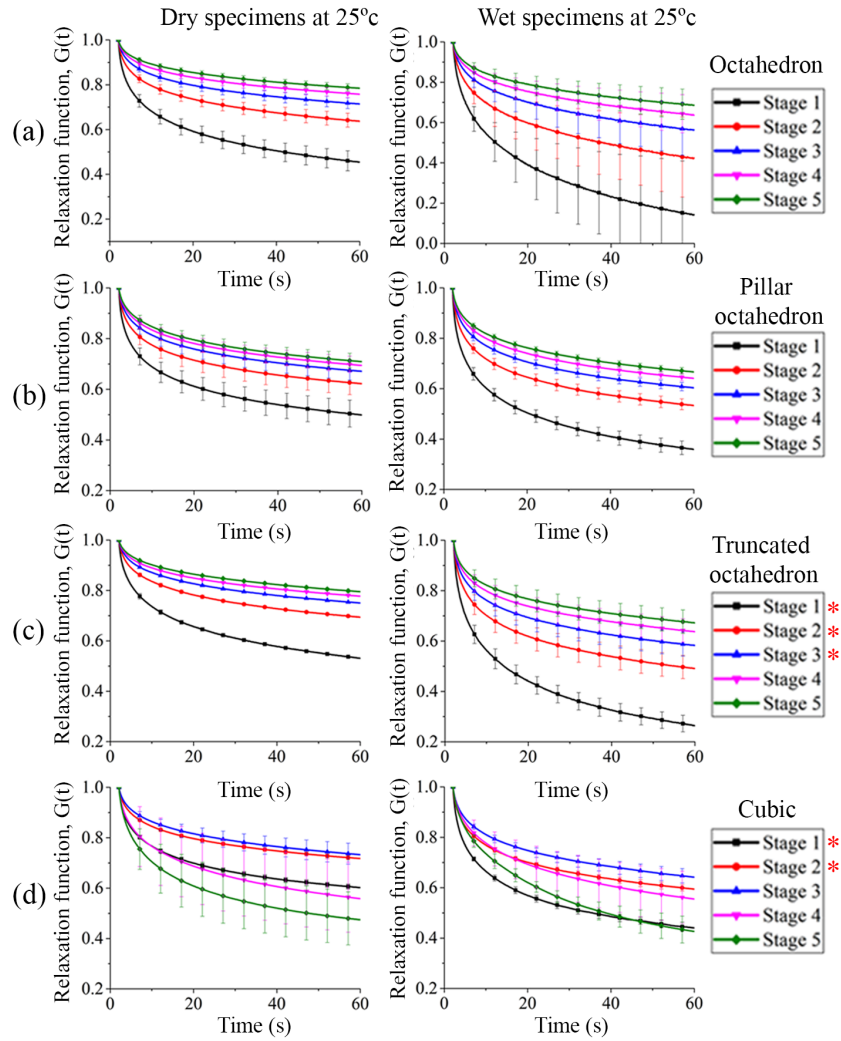
9

Fig. 9. Relaxation function G(t) of (a) octahedron, (b) pillar octahedron, (c) truncated octahedron, and (d) cubic shape under dry and wet conditions. (*) indicating a statistical difference between the dry and wet conditions.

3.3. Cell culture

Previous research suggested that over 60% porosity and pore sizes larger than 300 μm could promote bone formation and vascularization [10, 32]. In this work, the interconnected porous networks of 3DP cellular structures provide a pore size of 551 ± 55 μm and porosity of 74 ± 4%. Therefore, these structures are expected to be suitable for bone cell growth.

On the other hand, smaller pores may increase the surface area for protein adsorption, ion exchange, and bone-like apatite formation [10, 14]. With 3DP techniques, small pores can be created in the surface of polymer structures, especially when strut orientations aligned in angles [± 45°] with the printing direction, as adopted in the octahedron, pillar octahedron and truncated octahedron structures in this work. Another arguable thing is the retained wax after printing could be cytotoxic. However, Macdonald et al. reported the presence of wax coating on polymer surface is not harmful to the cells [33]. The possible reason is that the potential cell toxicity by ultra-fine particles (UFP) produced in incomplete photopolymerization can be mediated by the wax materials as physical barriers to diffusion. In this work, the pre-osteoblastic cells survival rate is 85 ± 4% in 7 days and no sign of cytotoxicity was observed, confirming the suitability as implant materials. SEM images confirmed pre-osteoblastic cell adhesion and proliferation on the specimen surfaces (Fig. 10). The pre-osteoblastic cell

morphology was compared in the different structures. The spindle-shape pre-osteoblasts, presented in networks were observed on the surfaces in all structures.
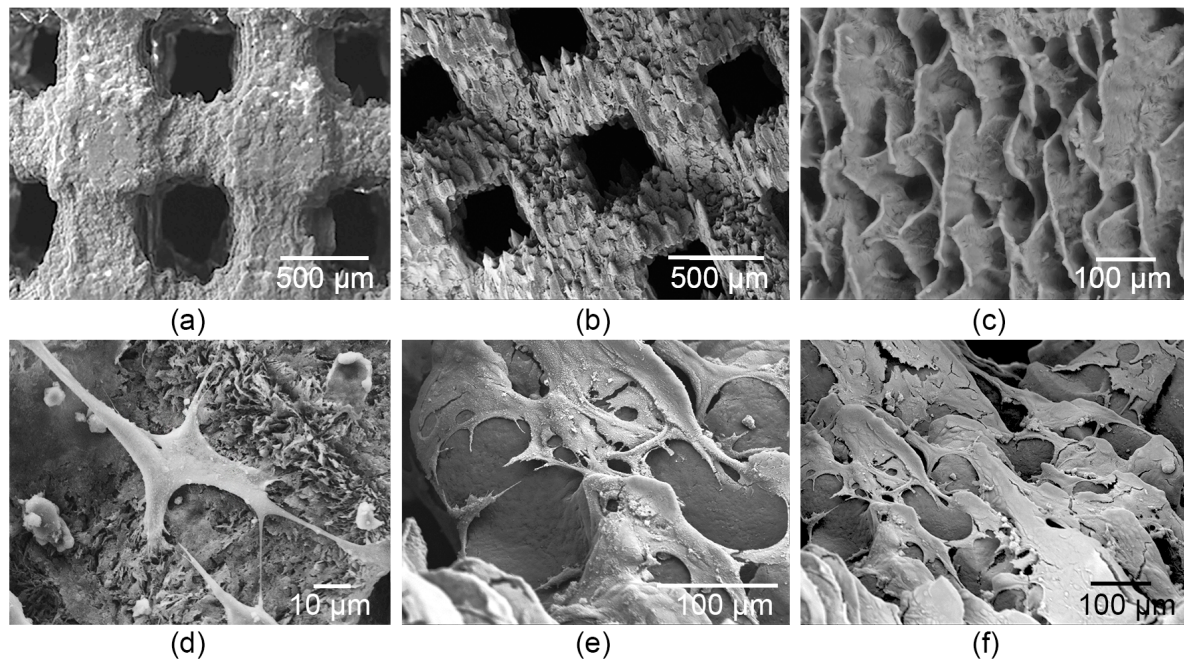

Fig. 10. SEM images showing surface roughness of (a) cubic and (b) octahedral unit cells, (c) Smaller pores (40 µm) on the surface after printing on the overhanging features, (d) cell adhesion and (e) and (f) cell coverage after 4 and 7 days.

The seeding efficiency (%) for each architectural design was calculated by taking into account the initial number of cells that were seeded to the scaffold and the numbers of cells that actually adhere to the scaffolds. Fig. 11a. shows that the internal architecture has an influence on cell seeding efficiency. Pre-osteoblastic cells were more likely to adhere to the octahedron (7.2%), pillar octahedron (5.1 %) and cubic (4.4 %) rather than truncated octahedral shape (3.7%). However, only the comparison between the octahedron and truncated octahedron was significant ($p = 0.02$). Surface hydrophilicity of a polymer is important for homogeneous and sufficient cell seeding and growth [34]. Polyurethane acrylate has better wettability than the surface of electrospun PCL, measured through water contact angle testing (70° vs 123°) [34, 35]. However, the seeding efficiency of this study was less than that of the electrospun PCL scaffolds [36]. This highlights the effect of architectures on seeding efficiency. As the pore size and porosity of each design are similar, the difference in seeding efficiency could be attributed to the flow characteristics and different surface roughness related to individual unit geometry. Unit geometry directly controls the tortuosity, a measure of flow distance that travels in the porous materials [37]. The strut intersection in the middle of octahedral type diverts the fluid from the straight direction and slows the flow rate. The low flow rate when pipetting a cell suspension onto the octahedral and pillar octahedral shapes would favor cell adherence, while the high flow rates of cubic and truncated octahedral shape contribute to cell deposition at the bottom of the well. In addition, the greater seeding efficiency of the ± 45° typed structures than the cubic type could be explained by the greater porous surfaces of the overhanging features fabricated with 3DP, Fig. 10.
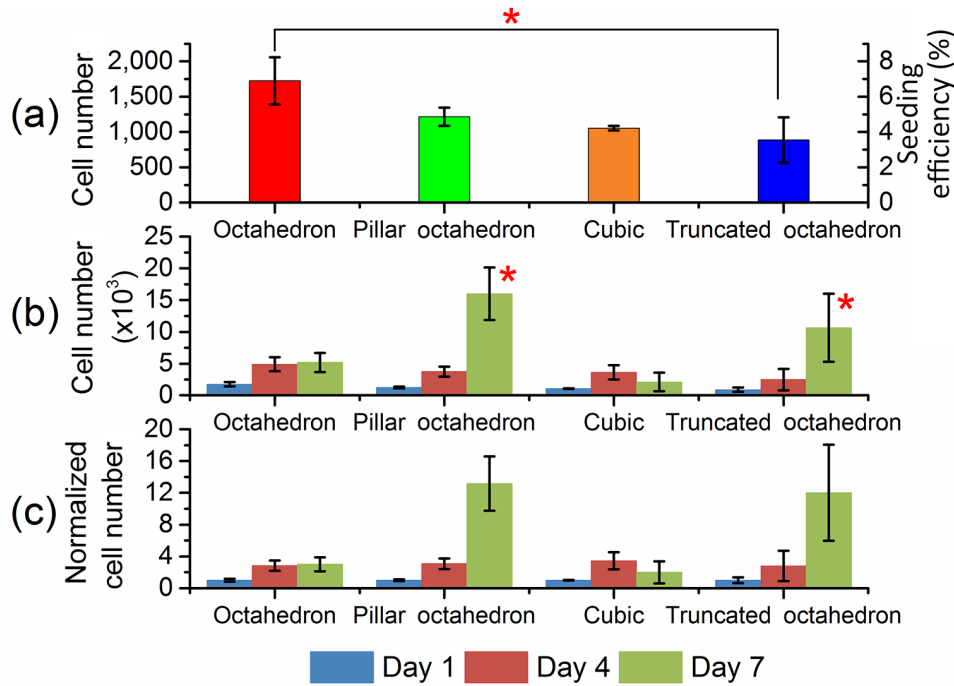
Fig. 11. (a) The numbers of pre-osteoblastic cells attached to the different cellular structures, (b & c) comparison the rates of cell proliferation within 7 days after cell seeding.

Cell proliferation test was conducted in all cellular structures. DNA content analysis was used to identify the number of growing cells. To compare the proliferation rates between the different structures, cell number was normalized using the number of attached cells at different times divided by the number of cells attached on day 1. Although high data scatter was observed, the pre-osteoblastic cells proliferated are significantly faster in the pillar octahedral and truncated octahedral structures on day 7 ($p < 0.01$), Fig. 11b. The greater cell proliferation of the pillar octahedron and truncated octahedron could be attributed to the greater surface areas of these polyhedral structures, compared with the cubic and octahedron.

As observed in this work, high relative density and lower porosity in a cellular structure can lead to increased strength and stiffness, consistent with previous reports [38, 39]. It is interesting to note that the mechanical response from a cellular structure depends on the loading modes. To this end, for axially loaded applications such as bone implants to fix long-bone defects, the cubic structure is the best choice because of its high stiffness under compressive force. High fatigue life under compression loading was observed in cubic unit cells [17, 39]. On the other hand, when subjected to a combined loading (compression, shear and torsion) such as femoral hip implants, the pillar octahedron is an appropriate architecture as it provides the greatest shear and torsional stiffness and high compressive stiffness. Note that the pillar octahedral structure also has the greatest accumulated stress during the stress relaxation test. Together with its better cell proliferation rate, pillar octahedral structure has demonstrated balanced mechanical and biological properties.

4. Conclusion

Using 3DP techniques, we have successfully fabricated 3D cellular structures with precisely controlled internal architectures. Combined small and large pores (40~550 μm) and high porosity of 74 % have been achieved. The internal structures play a key role in determining the overall mechanical and biological performance. The cubic structure [0° ± 90°] has much higher compression stiffness but lower shear and torsion stiffness than that in octahedron type structures [± 45°]. The pillar octahedron structure, combined the strut

12

characteristics featured along 0° and ± 45°, demonstrate high compression, shear and torsional stiffness (26.94 MPa, 18.93 MPa and 9.52 MPa, respectively). A reduction in stiffness has been observed in wet condition due to relaxation of the polymer. However, the pillar octahedron structure is insensitive to the wet condition. The structures with ± 45° strut alignments tends to increase the cell adherence due to higher porous surfaces. The greater surface areas of pillar octahedral structure significantly increase pre-osteoblastic cell proliferation than other structures. Therefore, the pillar octahedron is considered to have balanced mechanical and biological properties. We believe these findings may benefit the design and fabrication of advanced implants.

Acknowledgements

Formatting of funding sources

References

[1] Q.L. Loh, C. Choong, Three-dimensional scaffolds for tissue engineering applications: Role of porosity and pore size, Tissue Engineering - Part B: Reviews 19(6) (2013) 485-502.

[2] V. Karageorgiou, D. Kaplan, Porosity of 3D biomaterial scaffolds and osteogenesis, Biomaterials 26(27) (2005) 5474-5491.

[3] D.W. Hutmacher, M. Sittinger, M.V. Risbud, Scaffold-based tissue engineering: Rationale for computer-aided design and solid free-form fabrication systems, Trends in Biotechnology 22(7) (2004) 354-362.

[4] N. Sudarmadji, J.Y. Tan, K.F. Leong, C.K. Chua, Y.T. Loh, Investigation of the mechanical properties and porosity relationships in selective laser-sintered polyhedral for functionally graded scaffolds, Acta Biomaterialia 7(2) (2011) 530-537.

[5] N. Sudarmadji, C.K. Chua, K.F. Leong, The development of computer-aided system for tissue scaffolds (CASTS) system for functionally graded tissue-engineering scaffolds, in: M.A.K. Liebschner (Ed.) 2012, pp. 111-123.

[6] B.D. Ulery, L.S. Nair, C.T. Laurencin, Biomedical applications of biodegradable polymers, J Polym Sci Part B 49(12) (2011) 832-864.

[7] S. Gogolewski, K. Gorna, Biodegradable polyurethane cancellous bone graft substitutes in the treatment of iliac crest defects, J. Biomed. Mater. Res. Part A 80(1) (2007) 94-101.

[8] A.M. Tarawneh, M. Wettergreen, M.A.K. Liebschner, Computer-aided tissue engineering: Benefiting from the control over scaffold micro-architecture, in: M.A.K. Liebschner (Ed.) 2012, pp. 1-25.

[9] S.M. Peltola, F.P.W. Melchels, D.W. Grijpma, M. Kellomäki, A review of rapid prototyping techniques for tissue engineering purposes, Annals of Medicine 40(4) (2008) 268-280.

[10] M.W. Naing, C.K. Chua, K.F. Leong, Y. Wang, Fabrication of customised scaffolds using computer-aided design and rapid prototyping techniques, Rapid Prototyping Journal 11(4) (2005) 249-259.

[11] J. Kadkhodapour, H. Montazerian, A. Darabi, A.P. Anaraki, S.M. Ahmadi, A.A. Zadpoor, S. Schmauder, Failure mechanisms of additively manufactured porous biomaterials: Effects of porosity and type of unit cell, Journal of the Mechanical Behavior of Biomedical Materials 50 (2015) 180-191.

[12] S.M. Giannitelli, D. Accoto, M. Trombetta, A. Rainer, Current trends in the design of scaffolds for computer-aided tissue engineering, Acta Biomaterialia 10(2) (2014) 580-594.

[13] J.M. Williams, A. Adewunmi, R.M. Schek, C.L. Flanagan, P.H. Krebsbach, S.E. Feinberg, S.J. Hollister, S. Das, Bone tissue engineering using polycaprolactone scaffolds fabricated via selective laser sintering, Biomaterials 26(23) (2005) 4817-4827.

[14] K.F. Leong, C.M. Cheah, C.K. Chua, Solid freeform fabrication of three-dimensional scaffolds for engineering replacement tissues and organs, Biomaterials 24(13) (2003) 2363-2378.

[15] C. Mota, D. Puppi, F. Chiellini, E. Chiellini, Additive manufacturing techniques for the production of tissue engineering constructs, J Tissue Eng Regen Med 9(3) (2015) 174-190.

[16] M.A. Wettergreen, B.S. Bucklen, B. Starly, E. Yuksel, W. Sun, M.A.K. Liebschner, Creation of a unit block library of architectures for use in assembled scaffold engineering, CAD Computer Aided Design 37(11) (2005) 1141-1149.

[17] K. Hazlehurst, C.J. Wang, M. Stanford, Evaluation of the stiffness characteristics of square pore CoCrMo cellular structures manufactured using laser melting technology for potential orthopaedic applications, Materials & Design 51(0) (2013) 949-955.

[18] J. Wieding, R. Souffrant, W. Mittelmeier, R. Bader, Finite element analysis on the biomechanical stability of open porous titanium scaffolds for large segmental bone defects under physiological load conditions, Medical Engineering & Physics 35(4) (2013) 422-432.

[19] L. Mullen, R.C. Stamp, W.K. Brooks, E. Jones, C.J. Sutcliffe, Selective Laser Melting: A regular unit cell approach for the manufacture of porous, titanium, bone in-growth constructs, suitable for orthopedic applications, Journal of Biomedical Materials Research Part B: Applied Biomaterials 89B(2) (2009) 325-334.

[20] B. Gorny, T. Niendorf, J. Lackmann, M. Thoene, T. Troester, H.J. Maier, In situ characterization of the deformation and failure behavior of non-stochastic porous structures processed by selective laser melting, Materials Science and Engineering A 528(27) (2011) 7962-7967.

[21] S.M. Ahmadi, G. Campoli, S. Amin Yavari, B. Sajadi, R. Wauthle, J. Schrooten, H. Weinans, A.A. Zadpoor, Mechanical behavior of regular open-cell porous biomaterials made of diamond lattice unit cells, Journal of the Mechanical Behavior of Biomedical Materials 34 (2014) 106-115.

[22] M. Smith, Z. Guan, W.J. Cantwell, Finite element modelling of the compressive response of lattice structures manufactured using the selective laser melting technique, Int J Mech Sci 67 (2013) 28-41.

[23]

[24] C. Öhman, M. Baleani, E. Perilli, E. Dall'Ara, S. Tassani, F. Baruffaldi, M. Viceconti, Mechanical testing of cancellous bone from the femoral head: Experimental errors due to off-axis measurements, Journal of Biomechanics 40(11) (2007) 2426-2433.

[25] M. Viana, P. Jouannin, C. Pontier, D. Chulia, About pycnometric density measurements, Talanta 57(3) (2002) 583-593.

[26] P.A. Webb, Volume and Density Determinations for Particle Technologists, Micromeritics Instrument Corp (2001).

[27] B.K. Paul, S. Baskaran, Issues in fabricating manufacturing tooling using powder-based additive freeform fabrication, Journal of Materials Processing Technology 61(1-2) (1996) 168-172.

[28] M.A. Wettergreen, B.S. Bucklen, W. Sun, M.A.K. Liebschner, Computer-aided tissue engineering of a human vertebral body, Annals of Biomedical Engineering 33(10) (2005) 1333-1343.

[29] L.J. Gibson, Biomechanics of cellular solids, Journal of Biomechanics 38(3) (2005) 377-399.

[30] V. Sethuraman, K. Makornkaewkeyoon, A. Khalf, S.V. Madihally, Influence of scaffold forming techniques on stress relaxation behavior of polycaprolactone scaffolds, J. Appl. Polym. Sci. 130(6) (2013) 4237-4244.

[31] V.C. Mow, R. Huiskes, Basic orthopaedic biomechanics & mechano-biology, Lippincott Williams & Wilkins, Philadelphia, PA, 2005.

[32] R. Akbarzadeh, J.A. Minton, C.S. Janney, T.A. Smith, P.F. James, A.M. Yousefi, Hierarchical polymeric scaffolds support the growth of MC3T3-E1 cells, Journal of materials science. Materials in medicine 26(2) (2015) 116.

[33] N.P. Macdonald, F. Zhu, C.J. Hall, J. Reboud, P.S. Crosier, E.E. Patton, D. Wlodkowic, J.M. Cooper, Assessment of biocompatibility of 3D printed photopolymers using zebrafish embryo toxicity assays, LAB ON A CHIP 16(2) (2016) 291-297.

[34] M. Alishiri, A. Shojaei, M.J. Abdekhodaie, Biodegradable polyurethane acrylate/HEMA-grafted nanodiamond composites with bone regenerative potential applications: Structure, mechanical properties and biocompatibility, RSC Adv. 6(11) (2016) 8743-8755.

[35] A.K. Bassi, J.E. Gough, M. Zakikhani, S. Downes, The chemical and physical properties of poly(ε-caprolactone) scaffolds functionalised with poly(vinyl phosphonic acid-co-acrylic acid), J. Tissue Eng. 2(1) (2011) 1-9.

[36] J.M. Sobral, S.G. Caridade, R.A. Sousa, J.F. Mano, R.L. Reis, Three-dimensional plotted scaffolds with controlled pore size gradients: Effect of scaffold geometry on mechanical performance and cell seeding efficiency, Acta Biomaterialia 7(3) (2011) 1009-1018.

[37] A. Eshghinejadfard, L. Daróczy, G. Janiga, D. Thévenin, Calculation of the permeability in porous media using the lattice Boltzmann method, International Journal of Heat and Fluid Flow.

[38] R. Gümrük, R.A.W. Mines, S. Karadeniz, Static mechanical behaviours of stainless steel micro-lattice structures under different loading conditions, Materials Science and Engineering A 586 (2013) 392-406.

[39] S. Amin Yavari, S.M. Ahmadi, R. Wauthle, B. Pouran, J. Schrooten, H. Weinans, A.A. Zadpoor, Relationship between unit cell type and porosity and the fatigue behavior of selective laser melted meta-biomaterials, Journal of the Mechanical Behavior of Biomedical Materials 43 (2015) 91-100.